Electron-beam induced transformations of layered tin dichalcogenides

Sutter, E.; Huang, Y.; Komsa, H.-P.; Ghorbani-Asl, M.; Krasheninnikov, A. V.; Sutter, P.;

Originally published:

June 2016

Nano Letters 16(2016), 4410-4416

DOI: https://doi.org/10.1021/acs.nanolett.6b01541

Electron-Beam Induced Transformations of Layered Tin Dichalcogenides

Journal:	*Nano Letters*
Manuscript ID	nl-2016-01541j.R1
Manuscript Type:	Communication
Date Submitted by the Author:	27-May-2016
Complete List of Authors:	Sutter, Eli; University of Nebraska-Lincoln, Department of Mechanical and Materials Engineering Huang, Yuan; BNL, Komsa, Hannu-Pekka; University of Helsinki, Department of Physics Ghorbani-Asl, Mahdi; Helmholtz-Zentrum Dresden-Rossendorf, Krasheninnikov, Arkady; Aalto University, Department of Applied Physics, Aalto University Sutter, Peter; University of Nebraska-Lincoln, Electrical and Computer Engineering

Electron-Beam Induced Transformations of Layered Tin Dichalcogenides

E. Sutter,[1,] Y. Huang,[2] H.-P. Komsa,[3] M. Ghorbani-Asl,[4] A.V. Krasheninnikov,[3,4] and P. Sutter[5,*]*

[1]Department of Mechanical and Materials Engineering, University of Nebraska-Lincoln, Lincoln, NE 68588, USA

[2]Center for Functional Nanomaterials, Brookhaven National Laboratory, Upton, NY 11973, USA

[3]Department of Applied Physics, Aalto University, P.O. Box 11100, FI-00076 Aalto, Finland

[4]Institute of Ion Beam Physics and Materials Research, Helmholtz-Zentrum Dresden-Rossendorf, 01314 Dresden, Germany

[5]Department of Electrical and Computer Engineering, University of Nebraska-Lincoln, Lincoln, NE 68588, USA

Abstract

By combining high-resolution transmission electron microscopy and associated analytical methods with first-principles calculations, we study the behavior of layered tin dichalcogenides under electron beam irradiation. We demonstrate that the controllable removal of chalcogen atoms due to electron irradiation, at both room and elevated temperatures, gives rise to transformations in the atomic structure of Sn-S and Sn-Se systems so that new phases with different properties can be induced. In particular, rhombohedral layered SnS_2 and $SnSe_2$ can be transformed via electron beam induced loss of chalcogen atoms into highly anisotropic orthorhombic layered SnS and SnSe. A striking dependence of the layer orientation of the resulting SnS – parallel to the layers of ultrathin SnS_2 starting material, but slanted for transformations of thicker few-layer SnS_2 – is rationalized by a transformation pathway in which vacancies group into ordered S-vacancy lines, which convert via a Sn_2S_3 intermediate to SnS. Absence of a stable Sn_2Se_3 intermediate precludes this pathway for the selenides, hence $SnSe_2$ always transforms into basal plane oriented SnSe. Our results provide microscopic insights into the transformation mechanism and show how irradiation can be used to tune the properties of layered tin chalcogenides for applications in electronics, catalysis, or energy storage.

Keywords: Two-dimensional materials, defects, electron irradiation, structural transformation, sulfide, selenide.

*To whom correspondence should be addressed, E-Mail: psutter@unl.edu; esutter@unl.edu.

Layered metal chalcogenides have attracted intense interest as a group of mostly semiconducting two-dimensional (2D) and few-layer materials complementing other 2D systems, such as graphene or h-BN. Transition metal dichalcogenides (TMDs), the materials studied primarily so far, can crystallize in several polymorphs with different electronic structure. For example, in addition to the semiconducting trigonal prismatic ground-state structure MoS_2 can occur in a higher-energy octahedral 1T phase or a distorted 1T' variant, both of which are metallic.[1] The different phases are sufficiently close in energy that they can be interconverted by relatively mild treatments, such as charge transfer during alkali-metal intercalation,[2-4] substitutional doping,[5, 6] plasmonic hot electrons,[7] or by applying high pressure.[8] Electron irradiation in transmission electron microscopy (TEM) has been used to induce point defects (e.g., sulfur-vacancies)[9-11] and line defects in TMDs,[12] and to reversibly switch between the 2H, 1T, and 1T' phases of MoS_2.[3, 13] Whereas for TMDs multiple competing phases exist at constant composition (MX_2), other 2D or layered metal chalcogenides can show several stable phases with different stoichiometry. For the tin chalcogenides, stable layered crystal phases are known with Sn in Sn(IV) [SnS_2, $SnSe_2$] and Sn(II) [SnS, SnSe] oxidation states. For SnS_2, an n-type semiconductor with an indirect bandgap of ~2.2 eV,[14, 15] high-mobility field-effect transistors with large on-off current ratios have recently been demonstrated.[15-17] SnS and SnSe, both of which have anisotropic (orthorhombic) layered structures that represent compound analogues of black phosphorus,[18] show promise for photovoltaic energy conversion[19] as well as extraordinary thermoelectric properties.[20]

Several methods have been used to produce SnS (SnSe).[19, 21-24] The ability of high-energy electrons to induce atomic displacements in few-layer materials (especially for

light elements, for recent reviews see Refs. 25, 26) together with the existence of stable Sn sulfide (selenide) structures with different chalcogen content raises the possibility that layered Sn-dichalcogenides could be controllably converted to monochalcogenides.[27] *In-situ* TEM experiments may be used to study the transformation pathway, the configuration and stability of possible intermediates, as well as the final phases with near-atomic resolution. When combined with *ab-initio* calculations, such atomic-scale experiments can provide a detailed understanding of defect formation and interaction mechanisms, as well as phase interconversion pathways in layered crystals and can support the development of strategies for preparing high-quality Sn(II)-chalcogenides or SnS_2/SnS ($SnSe_2$/SnSe) heterostructures via controlled S (Se) removal from Sn(IV)-chalcogenide starting materials.

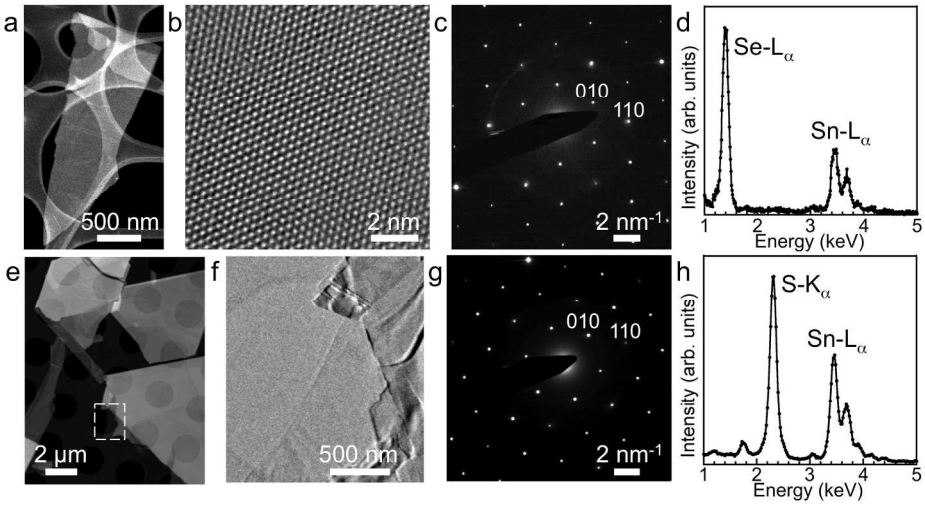

Figure 1 – Few-layer $SnSe_2$ (top row) and SnS_2 (bottom row). a, e, f. Low-magnification HAADF-STEM image of $SnSe_2$ (a) and SnS_2 flakes (e), respectively, supported on holey carbon grids; and low-magnification TEM image of SnS_2 flakes (f). **b.** HR-TEM of the $SnSe_2$ lattice structure. **c, g.** Electron diffraction patterns along the [001] zone axis (ZA) perpendicular to the basal planes of $SnSe_2$ (c) and SnS_2 (g) layered crystals. **d, h.** EDS spectra of $SnSe_2$ (d) and SnS_2 (h).

Fig. 1 shows typical plan-view high-angle annular dark-field scanning TEM (HAADF-STEM) and high-resolution TEM (HR-TEM) images of few-layer $SnSe_2$ (Fig.

1 (a), (b)) and SnS_2 (Fig. 1 (e), (f)) exfoliated onto carbon supports. HAADF-STEM was used to identify areas with few-layer thickness (see also Supplementary Information, SI; Fig. S1). The high crystalline quality of $SnSe_2$ (and SnS_2) in thin areas is demonstrated in the HR-TEM image shown in Fig. 1b. Transmission electron diffraction patterns can be unambiguously indexed to $SnSe_2$ and SnS_2 along the [001] zone axis (ZA), respectively (Fig. 1 (c), (g)). Energy dispersive X-ray spectrometry (EDS) measurements (Fig. 1 (d), (h)) confirm the SnX_2 (X: S, Se) composition of the flakes.

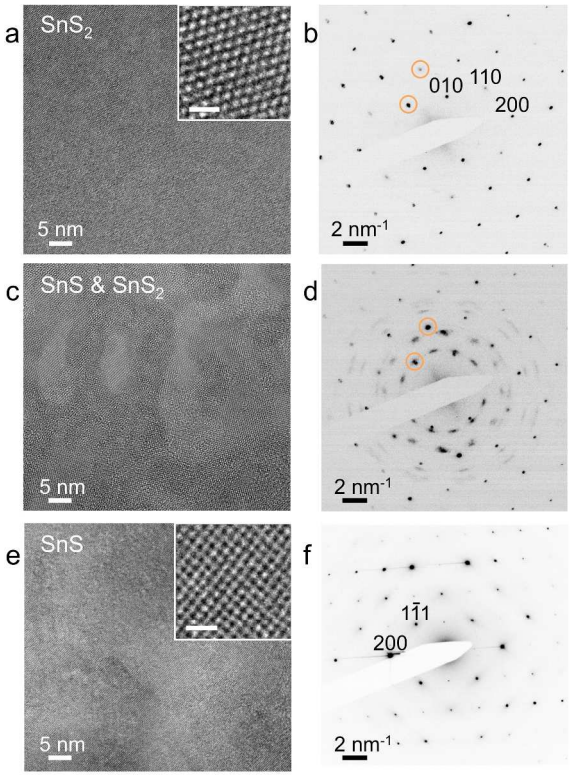

Figure 2. Evolution of few-layer SnS_2 under electron-beam irradiation. a. HR-TEM image of a thin area in a SnS_2 flake. **b.** Electron diffraction pattern showing the SnS_2 crystal structure along [001] zone axis (ZA). **c.** HR-TEM image of the same flake after 200 keV electron-beam exposure at room temperature for 12 minutes. **d.** Diffraction pattern showing a superposition of the original SnS_2 reflections and additional reflections that can be indexed to the orthorhombic α-SnS crystal structure. **e.** TEM image of the flake after 200 keV electron-beam exposure at 300°C for 36 minutes. **f.** Diffraction pattern indexed to single crystalline orthorhombic α-SnS crystal structure along the [011] ZA. Scale bars of panel a, e. insets: 1 nm.

To investigate electron-beam induced structural transformations, SnS_2 and $SnSe_2$ flakes with an initial thickness of 9-10 layers were used as starting materials (for a description of the thickness measurement, see Methods). Below, we discuss primarily the transformation of SnS_2. Unless noted otherwise, analogous behavior was found for the corresponding selenides (see SI). The time-dependent structural evolution of a characteristic SnS_2 flake under the electron beam is shown in supplementary movie M1 (see also Fig. 2; Fig. S2). Initially, the flake is single-crystalline SnS_2, as seen in HR-TEM (Fig. 2 (a)) and electron diffraction (Fig. 2 (b)), which shows only one family of spots that can be indexed to SnS_2 along the [001] ZA. With increasing observation time (electron dose) the HR-TEM contrast changes. First the SnS_2 lattice fringes appear to become disordered, followed by the emergence of small areas with different lattice fringes indicating a change in crystal structure (Fig. 2 (c)). At the same time, new spots appear in the diffraction pattern, which can be indexed to the SnS crystal structure (Fig 2 (d)). The presence of diffraction spots from both the original SnS_2 structure and the newly formed SnS confirms that the flake now contains SnS_2 and SnS domains. At this stage, the individual SnS domains are small but locally show high crystallinity. Further electron irradiation leads to the complete transformation of the SnS_2 flake into SnS. The structural transformation of few-layer SnS_2 flakes was observed for all electron energies (80, 200, and 300 keV) and beam currents used in this study. The electron-irradiation driven transformation at room temperature gives rise to smaller monocrystalline SnS flakes (~5-10 nm). Annealing at moderate temperatures between 200°C and 400°C promotes the formation of large single crystalline SnS areas (Fig. 2 (e); Fig. 4). After completion of the transformation, the diffraction pattern (Fig. 2 (f)) again shows a single

family of spots that can be indexed to SnS along the [011] ZA.

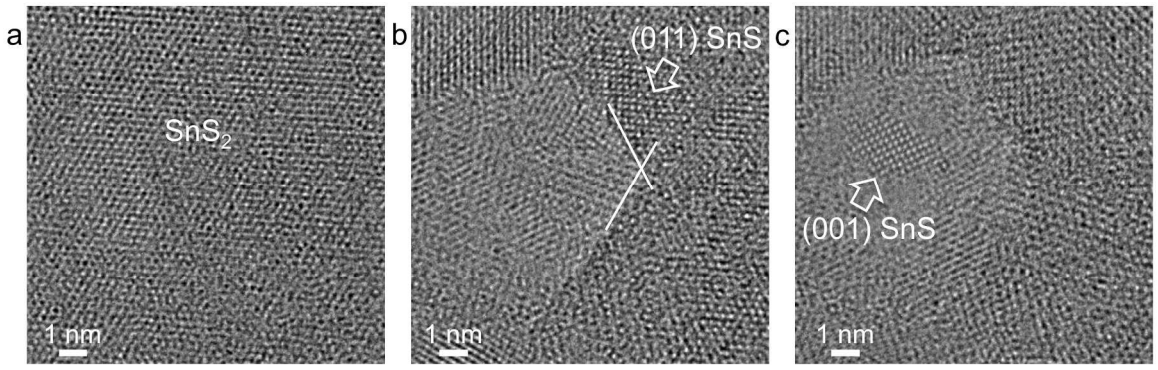

Figure 3. Electron-beam induced thinning of SnS_2 and transformation of ultrathin SnS_2 to (001) SnS. a. Initial few-layer SnS_2 crystal. **b.** Simultaneous local thinning and transformation of thicker (001) SnS_2 to off-axis (011) SnS (arrow). **c.** Transformation of ultrathin (001) SnS_2 to (001) SnS (arrow).

The initial SnS_2 flakes consist of covalently bonded S-Sn-S layers held together by weak interlayer forces. In plan-view TEM, the SnS_2 flakes resting on carbon support are viewed along the [001] direction (c-axis). The product of the electron-induced transformation of few-layer SnS_2, obtained after the loss of ~50% of the original sulfur content, are SnS layers viewed such that the electron beam projects along the [011] direction. Strikingly, this implies that the weakly coupled SnS layers are no longer stacked along the surface normal, but they are tilted by ~21 degrees relative to the plane of the original SnS_2 layers. Simultaneously with the transformation of few-layer SnS_2 into SnS, we observe that the original flakes get progressively thinner in certain areas, i.e., their thickness is no longer homogeneous (Fig. 3; supplementary movie M2). Local thinning starts in small areas (Fig. 3 (a)) that expand by the propagation of a well-defined front separating thinner material from the surrounding thicker areas of the flake. The thinning front comprises straight sections that propagate along the $[\bar{1}00]$ and the [010] directions within the (001) plane of the SnS_2 flake. Once some of these areas become

very thin, they also show a structural transformation to a less sulfur-rich tin sulfide polymorph (Fig. 3 (c)). In this delayed transformation, ultrathin sections of SnS_2 again convert to ordered SnS. But now the emerging ultrathin SnS is c-axis (i.e., [001]) oriented, i.e., the layer plane is parallel to the support (and to the original SnS_2 layers).

At higher temperatures, the electron-beam induced transformation proceeds similar to that at room temperature, but it clearly shows signatures of longer-range mass transport, notably in the size and homogeneity of the resulting products (Fig. S3). Areas converted to SnS are much larger in size, reaching up to several hundred nm (Fig. S3 (a), (b)), and show uniform thickness, composition, and lattice orientation as well as long-range crystalline order (Fig. S3 (c)). The faceted edges of the transformed flakes include primarily 90° angles, consistent with the orthorhombic structure of SnS. Electron diffraction (Fig. S3 (d), (e)) confirms a uniform transformation of extended areas into a single-crystalline, 21° off-axis (i.e., [011]-oriented) layered SnS phase already found in the few-nanometer domains formed at room temperature. The regions that undergo thinning become larger and clearly show the hexagonal shape of the developing thin areas (Fig. S4).

In-situ observations at elevated temperature also clarify the further evolution of areas uniformly transformed to SnS during continued exposure to high-energy electrons (Fig. S5). Once large uniform SnS domains have been formed, their lateral dimensions shrink slightly with continued electron exposure (Fig. S5 (a), (b)). EDS composition measurements indicate that at the same time the thickness of the SnS domains is substantially reduced (Fig. S5 (c)), albeit at constant composition, i.e., with a net loss of both tin and sulfur at equal rates. This behavior is consistent with a high stability of the

Sn(II)-sulfide phase. The loss of Sn is enabled by both long-range diffusion (i.e., accumulation of Sn near the flake edges) and thermal evaporation at elevated temperatures.

The transformation from SnS_2 to SnS is clearly driven by irradiation by the electron beam. The impinging high-energy electrons can create defects through several mechanisms: ballistic displacement of atoms, chemical etching, electronic excitation, or their combination. All of these mechanisms have been observed in other non-metallic 2D systems, e.g., h-BN layers.[28-30] For TMDs such as MoS_2 the primary defect formation pathway has been shown to be a loss of S atoms under electron irradiation.[9] The calculated displacement thresholds for chalcogen atoms in SnS_2 and $SnSe_2$ (Fig. S6) appear to be very similar to the ones for the TMDs. The threshold energies for sputtering are sufficiently low that the production of S-vacancies is possible at energies above 80 keV. Under prolonged irradiation, the progressive removal of S by knock-on sputtering causes a buildup of S-vacancies to levels at which the original trigonal Sn-dichalcogenide structure is destabilized (Fig. 4 (a)). Density-functional theory (DFT) calculations indicate the presence of an Sn_2S_3 phase at intermediate S content between SnS_2 and SnS (see below). The structure of Sn_2S_3 can be thought of as a regular array of SnS_2 fragments, i.e., the loss of 25% of the original S atoms can be accommodated by breaking up of the original S-Sn-S layers into smaller, partially overlapping fragments that are stacked at alternating angles relative to the (001) planes of the SnS_2 flake (Fig. 4 (b)). Comparison of Fig. 4 (b) [Sn_2S_3] and Fig. 4 (c) [21°-tilted SnS, as observed experimentally] suggests that the tilted SnS phase can evolve by selecting one of the tilt angles of the overlapping segments that make up the Sn_2S_3 intermediate phase. This

pathway can explain why the layered SnS is not basal plane oriented, but arises with its layers tilted by ~21° off-axis. From the fact that electron diffraction does not show the [001] zone axis pattern of Sn_2S_3 (Fig. S7) for sufficiently large areas or long time periods to be detected experimentally we conclude that the Sn_2S_3 structure represents a local metastable phase that mediates the initial transformation to SnS, but does not exist as a long-lived, extended intermediate structure. In the electron-induced transformation of very thin SnS_2, finally, tilted few-layer SnS no longer represents the final state, but instead a basal-plane (c-axis) oriented SnS structure is formed (Fig. 3 (c); Fig. 4 (d)). This finding suggests that only SnS_2 above a critical thickness of ~3 layers can convert via an Sn_2S_3 intermediate into tilted SnS, whereas for thinner layered SnS_2 such an intermediate phase is geometrically suppressed and the sulfur-deficient crystal directly transforms into [001]-oriented SnS.

The transformation of $SnSe_2$ generally proceeds analogous to SnS_2, starting with disordering of the initially single crystalline $SnSe_2$ layers, followed by the appearance of the SnSe lattice structure (Fig. S8-S9). Once the transition to SnSe is completed, however, the individual layers are not tilted as in SnS but invariably align with the plane of the original $SnSe_2$ layers. This preference for formation of (basal plane) [001]-oriented SnSe (Fig. S9) suggests that an Sn_2Se_3 intermediate phase (i.e., the analogue of Sn_2S_3) does not exist for the Sn-Se system.

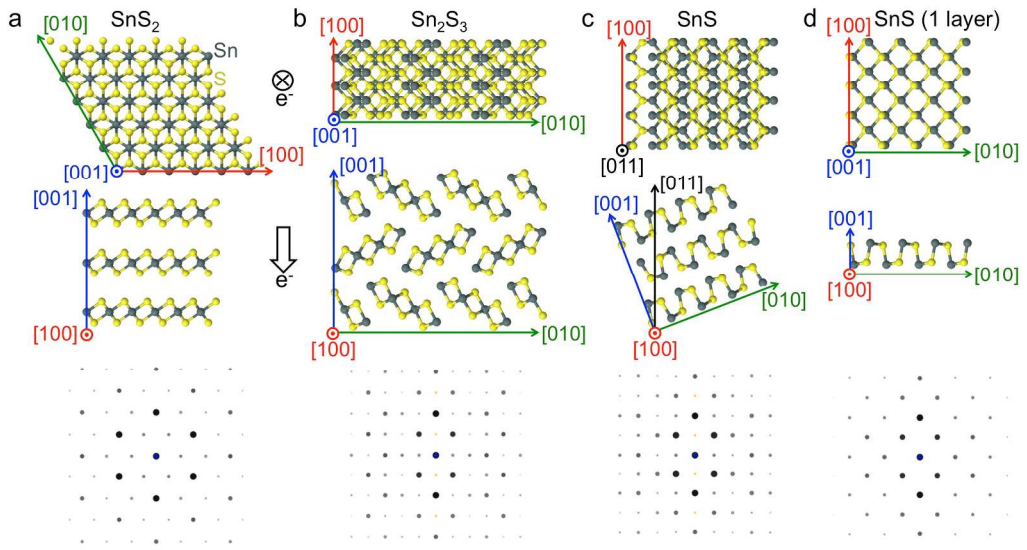

Figure 4. Comparison of structures and simulated diffraction patterns of SnS_2, Sn_2S_3, and SnS. a. SnS_2 layered structure viewed along the [001] and [100] direction, and simulated [001] ZA diffraction pattern. **b.** Sn_2S_3 viewed along [001] and [100] directions, and simulated [001] ZA diffraction pattern. **c.** Orthorhombic few-layer α-SnS viewed along the [011] and [100] directions, and [011] ZA diffraction pattern. **d.** c-axis oriented single-layer SnS viewed along the [001] and [100] directions, and [001] ZA diffraction pattern. The TEM viewing direction is perpendicular to the plan-view models (top row) and along the direction of the open arrow for the cross-section models (middle row). Note: hexagonal basis in (a); orthorhombic basis in (b)-(d).

Whereas the later stages of the $SnS_2 \rightarrow SnS$ transformation can be rationalized on the basis of the experimental observations (as summarized in Fig. 4), two important points require further clarification: (i) the pathway of the transformation from monocrystalline few-layer SnS_2 to the Sn_2S_3 intermediate; and (ii) the likely absence of a stable Sn_2Se_3 intermediate structure, which would explain the preference for a transformation of $SnSe_2$ to basal-plane oriented (001) SnSe. We addressed these questions via DFT calculations (see Methods).

Calculations were carried out for the three phases – SnX_2, Sn_2X_3, and SnX (where X: S, Se) – to determine their formation enthalpies. In order to properly account for the competition between van der Waals interaction and chemical bonding, we have adopted

the van der Waals functional revB86b, which has been shown to yield good lattice parameters and layer binding energies.[31, 32] The calculated formation enthalpies are shown in Table I, together with the energy difference for $Sn_2X_3 - (SnX_2+SnX)$.

Table I: Calculated formation enthalpies (in eV per formula unit) for bulk and single-layer tin sulfides and selenides.

	SnS	Sn_2S_3	SnS_2	$Sn_2S_3 - (SnS+SnS_2)$
Bulk	-1.10	-2.49	-1.36	-0.02
1L	-0.82	-2.00	-1.16	-0.03
	SnSe	Sn_2Se_3	$SnSe_2$	$Sn_2Se_3 - (SnSe+SnSe_2)$
Bulk	-0.98	-2.04	-1.08	+0.01
1L	-0.67	-1.53	-0.84	-0.02

For the tin sulfides, the Sn_2S_3 phase is stable over the SnS_2+SnS phase mixture, whereas in bulk tin selenides the Sn_2Se_3 phase is found to be unstable. This is consistent with experimental phase diagrams showing that Sn_2Se_3 does not exist under thermal equilibrium, whereas Sn_2S_3 does.[33, 34] Upon increasing temperature, the system should follow more closely the equilibrium energetics (assuming that the sputtering rate by the electron beam remains roughly constant). Indeed, larger areas of (011) SnS were obtained at higher temperatures.

Even though the evolution of the system is likely governed by the energetics of the phases, the actual transformation mechanism may be determined by the kinetics of the process. To this end, we also studied the kinetic pathway for the $SnS_2 \rightarrow Sn_2S_3$ transformation, and found it to be consistent with the picture based on energy considerations. Specifically, we found that the most probable kinetic pathway consists of two steps: First, vacancies created by electron-beam interactions are clustered into double vacancy lines; and second, the energy can be lowered by partially overlapping the "edges" on both sides of the vacancy line, i.e., formation of the Sn_2S_3 structure (Fig. 5).

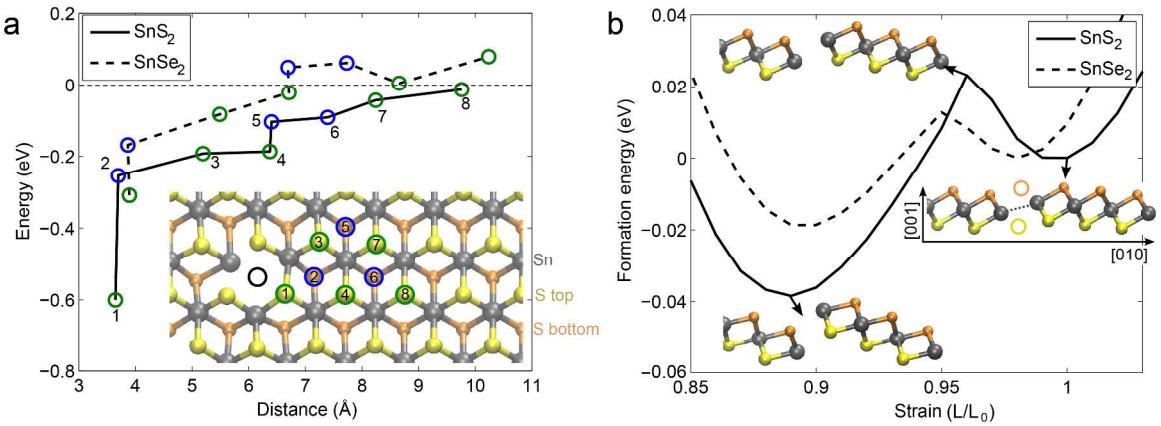

Figure 5. Kinetic pathway of the $SnS_2 \rightarrow Sn_2S_3$ transformation. (a) Formation energies for two vacancies as a function of their distance in SnS_2 and in $SnSe_2$. The corresponding positions in the SnS_2 lattice are illustrated in the lower right corner. Energies are given with respect to two isolated vacancies. **(b)** Energies of infinite double vacancy line as a function of the supercell length (strain) in the [010] direction in SnS_2 and $SnSe_2$. Selected atomic structures are also shown.

The calculated migration barriers for vacancy diffusion are 1.23 eV and 0.93 eV for SnS_2 and $SnSe_2$, respectively, indicating minor thermally activated diffusion at RT but significant diffusion already at 200°C. However, the diffusion may additionally be activated by collision with the relativistic electrons of the beam. In this case the kinetic energy transferred to Se is significantly smaller than that to S. The tendency toward clustering of the accumulated vacancies is quantified via the energy gain as a function of the vacancy distance, shown in Fig. 5 (a). In SnS_2, the vacancies are attracted to each other over a distance of about 8 Å. In $SnSe_2$ the attraction is weaker and more short-ranged, and there is even a repulsive interaction at intermediate distances. Taken together these results indicate that the vacancies in SnS_2 are more prone to clustering than in $SnSe_2$, and would thus limit the transformation process in $SnSe_2$. A comprehensive comparison between different vacancy cluster configurations is shown in the SI (Fig. S10). The lowest energy structure corresponds to double vacancy lines, such as could for instance be formed by removing atoms 1, 2, 4, 6, and 8 in Fig. 5 (a). Finally, if the sample

is allowed to contract along the [010] direction, the system can transform into the partially overlapping motif characteristic of the Sn_2S_3 structure (see Fig. 5 (b)).

2D and few-layer materials are usually assumed to adopt a configuration in which the layer plane is parallel to the support surface, although exceptions have been found. For example, it has been shown that the conversion of metallic Mo (and W) films to MoS_2 (WS_2) can lead to horizontal or vertical stacking of the resulting layered materials, depending on the metal film thickness.[35] Our results show that the transformation between different layered materials (here $SnS_2 \rightarrow SnS$) involves thickness-dependent configurations of the final SnS crystal – either with SnS layers parallel (for ultrathin SnS_2) or at an angle of ~21° to the starting SnS_2 planes (for thicker few-layer SnS_2) – which is explained by a pathway of the transformation via sulfur vacancy lines and a (local) Sn_2S_3 intermediate structure for sufficiently thick SnS_2, and suppression of that pathway for ultrathin SnS_2. Electronic structure and transport calculations show diverse properties of the materials addressed here. All of them are semiconductors with thickness-dependent (0.18–1.75 eV, Figs. S11, S12), primarily indirect bandgaps. The final products of the electron-beam induced transformations, SnS and SnSe, have direct bandgaps along the $\Gamma - X$ line in the Brillouin zone. Comparing the effective electron masses (m*, Table S4), we find low m* for SnS, suggesting high electron mobility in the phonon-scattering limited regime. Quantum transport calculations show a pronounced anisotropy in the in-plane conductance of Sn_2S_3, whereas basal-plane oriented SnS has anisotropic conductance within a narrower energy range and the conductance in SnS_2 is nearly perfectly isotropic, similar to TMDs such as MoS_2 (Fig. S14 and S15).[36] Anisotropic conductivity originates from the anisotropic atomic structure – especially

pronounced for Sn_2S_3 (covalent bonding along [100] *vs.* fragmented nanolayers along [010]) – which leads to different transmission pathways in the materials (Fig. S16). Similar to Sn_2S_3, a strongly anisotropic in-plane conductance can be expected also for the tilted few-layer SnS obtained here, since carrier transmission in one of the in-plane direction involves only covalent bonds whereas transport in the orthogonal direction requires the crossing of van der Waals gaps. Beyond the anisotropic electronic and transport properties, the ability to generate tilted layered crystals that expose extended arrays of edges at the surface may also be of interest for applications in catalysis or energy storage. For MoS_2-based catalysts, edges have been implicated as one of the primary active sites in reactions such as the hydrogen evolution reaction (HER),[37, 38] and materials that expose dense arrays of edges may provide enhanced catalytic activity. Energy storage related intercalation processes, finally, proceed most easily from exposed edges (e.g., in SnS_2 nanoflakes).[39-41] Layered structures such as the tilted SnS crystals demonstrated here maximize the accessibility of the interlayer space to intercalants, and may thus enable high charging and discharging rates in energy storage applications.

In conclusion, we used *in-situ* microscopy and *ab-initio* calculations to investigate electron beam induced transformations of few-layer SnS_2 and $SnSe_2$ to SnS and SnSe, respectively. Different transformation pathways dependent on flake thickness and for SnS_2 versus $SnSe_2$ produce different (001)- or tilted (011)-oriented, layered monochalcogenides. The transformations driven by a progressive chalcogen loss due to high-energy electron irradiation initially result in mixed mono- and dichalcogenides, followed by the complete conversion to SnS or SnSe. The controlled formation of SnX_2/SnX heterostructures may be possible by tuning the process conditions, including

electron exposure time, temperature, etc. Another route to heterostructures is to use local electron irradiation for transforming selected parts of a flake to the product polymorph. Conversions at elevated temperature produce large-scale homogeneous materials, i.e., a combination of thermal and electron-stimulated processes may provide high-quality ultrathin SnS (SnSe) for device applications. To this end, the mechanisms identified here should lend themselves to the conversion of layered crystals – tin chalcogenides and other systems that have stable polymorphs with different stoichiometry – in the range from monolayers up to larger thicknesses that still allow penetration by high-energy electrons and removal of the chalcogen atoms.

Materials and Methods

The starting materials used here were high-quality bulk crystals of layered SnS_2 and $SnSe_2$, grown by the vertical Bridgman method as described previously.[42] The layered bulk crystals were exfoliated into thinner flakes, including few-layer and single-layer SnS_2 and $SnSe_2$ according to the methods described in Ref. [43]. Transmission electron microscopy (TEM) was performed in several modes, high-angle annular dark-field scanning TEM (HAADF-STEM) and high-resolution TEM (HR-TEM), selected-area diffraction, and energy-dispersive X-ray spectroscopy (EDS) in two microscopes, a JEOL 2100F and a FEI Titan 80-300 microscope equipped with a CEOS Cs-corrector and Gatan K2-IS *in-situ* direct detection (DDD) camera. Both microscopes were equipped with Gatan 652 high-temperature sample holders used for annealing experiments. Plan-view TEM samples were prepared by exfoliating SnS_2 or $SnSe_2$ flakes from bulk crystals directly onto holey carbon TEM grids. The thickness of few-layer SnS_2 flakes on SiO_2/Si supports can be determined precisely using optical microscopy.[15] To determine the number of layers for flakes supported on carbon films used in TEM investigations, the absolute thickness was calibrated by counting the layers in cross-sectional images obtained in areas where flake edges were spontaneously folded during exfoliation (Fig S1 (a)). The thickness in other areas was determined by measuring the thickness-dependent attenuation of the electron beam current by a flake compared to the non-attenuated current measured through vacuum (I_{vacuum} : $I_{on\ flake}$, see Fig. S1 (b)). TEM observations were carried out at electron energies of 200 keV (JEOL 2100F), 80 keV and 300 keV (FEI Titan 80-300), beam current densities ~20 pA/cm^2, and temperatures between 20°C and 400°C. Time-resolved imaging was performed with a Gatan K2-IS DDD camera at 2.5 milliseconds per frame time resolution. During imaging, the DDD camera outputs

binary files to a workstation equipped with solid-state hard-drives. 2k×2k images were extracted at 400 frames per second from these binary files using Digital Micrograph software. Movies shown in the Supplementary Information were generated by merging every 100th image from these sequences, and are played at 10 frames per second.

Density-functional theory calculations were carried out in the plane-wave basis and within the projector-augmented wave (PAW) description of the core regions, as implemented in the VASP code.[44, 45] In the calculations for pristine systems, we used 500 eV cutoff and k-point resolution of 0.18 1/Å or better, and compared four exchange-correlation functional: LDA, PBE, PBE-D2, and revB86b.[32, 46-48] Defect clustering was studied within an 8x8 supercell, Γ-point sampling of the Brillouin zone, and with the VASP nominal cutoff of 280 eV for SnS_2 and 212 eV for $SnSe_2$. For computational details for electronic structure and transport calculations, see Supplementary Information.

Acknowledgements

This research used resources of the Center for Functional Nanomaterials, which is a U.S. DOE Office of Science Facility at Brookhaven National Laboratory under Contract No. DE-SC0012704. PS and ES acknowledge support by the U.S. Department of Energy, Office of Basic Energy Sciences, Division of Materials Sciences and Engineering. AVK and HPK acknowledge support from the US Army RDECOM, contract No. W911NF-15-1-0606, and Academy of Finland through Projects No. 263416 and 286279 and Centres of Excellence Programme (2012-2017) under Project No. 251748. We also thank CSC–IT Center for Science Ltd. and Aalto Science-IT project for generous grants of computer time.

Supporting Information Available. Supplementary Figures S1–S16; Supplementary Tables S1–S4; Supplementary Movies M1–M2; Computational details for electronic structure and transport calculations; Supplementary References. This material is available free of charge via the Internet at http://pubs.acs.org.

Note: The authors declare no competing financial interest.

References

1. Chhowalla, M.; Shin, H. S.; Eda, G.; Li, L.-J.; Loh, K. P.; Zhang, H. *Nat Chem* **2013,** 5, (4), 263-275.
2. Py, M. A.; Haering, R. R. *Canadian Journal of Physics* **1983,** 61, (1), 76-84.
3. Wang, L.; Xu, Z.; Wang, W.; Bai, X. *Journal of the American Chemical Society* **2014,** 136, (18), 6693-6697.
4. Xiong, F.; Wang, H.; Liu, X.; Sun, J.; Brongersma, M.; Pop, E.; Cui, Y. *Nano Letters* **2015,** 15, (10), 6777-6784.

5. Enyashin, A. N.; Yadgarov, L.; Houben, L.; Popov, I.; Weidenbach, M.; Tenne, R.; Bar-Sadan, M.; Seifert, G. *The Journal of Physical Chemistry C* **2011,** 115, (50), 24586-24591.
6. Kappera, R.; Voiry, D.; Yalcin, S. E.; Branch, B.; Gupta, G.; Mohite, A. D.; Chhowalla, M. *Nature Materials* **2014,** 13, (12), 1128-1134.
7. Kang, Y.; Najmaei, S.; Liu, Z.; Bao, Y.; Wang, Y.; Zhu, X.; Halas, N. J.; Nordlander, P.; Ajayan, P. M.; Lou, J.; Fang, Z. *Advanced Materials* **2014,** 26, (37), 6467-6471.
8. Nayak, A. P.; Bhattacharyya, S.; Zhu, J.; Liu, J.; Wu, X.; Pandey, T.; Jin, C.; Singh, A. K.; Akinwande, D.; Lin, J.-F. *Nat Commun* **2014,** 5.
9. Komsa, H.-P.; Kotakoski, J.; Kurasch, S.; Lehtinen, O.; Kaiser, U.; Krasheninnikov, A. V. *Physical Review Letters* **2012,** 109, (3), 035503.
10. Lin, Y.-C.; Björkman, T.; Komsa, H.-P.; Teng, P.-Y.; Yeh, C.-H.; Huang, F.-S.; Lin, K.-H.; Jadczak, J.; Huang, Y.-S.; Chiu, P.-W.; Krasheninnikov, A. V.; Suenaga, K. *Nature Communications* **2015,** 6.
11. Zhou, W.; Zou, X.; Najmaei, S.; Liu, Z.; Shi, Y.; Kong, J.; Lou, J.; Ajayan, P. M.; Yakobson, B. I.; Idrobo, J.-C. *Nano Letters* **2013,** 13, (6), 2615-2622.
12. Komsa, H.-P.; Kurasch, S.; Lehtinen, O.; Kaiser, U.; Krasheninnikov, A. V. *Physical Review B* **2013,** 88, (3), 035301.
13. Lin, Y.-C.; Dumcenco, D. O.; Huang, Y.-S.; Suenaga, K. *Nature Nanotechnology* **2014,** 9, (5), 391-396.
14. George, J.; Joseph, K. S. *Journal of Physics D: Applied Physics* **1982,** 15, (6), 1109.
15. Huang, Y.; Sutter, E.; Sadowski, J. T.; Cotlet, M.; Monti, O. L. A.; Racke, D. A.; Neupane, M. R.; Wickramaratne, D.; Lake, R. K.; Parkinson, B. A.; Sutter, P. *ACS Nano* **2014,** 8, (10), 10743-10755.
16. Song, H. S.; Li, S. L.; Gao, L.; Xu, Y.; Ueno, K.; Tang, J.; Cheng, Y. B.; Tsukagoshi, K. *Nanoscale* **2013,** 5, (20), 9666-9670.
17. Pan, T. S.; De, D.; Manongdo, J.; Guloy, A. M.; Hadjiev, V. G.; Lin, Y.; Peng, H. B. *Applied Physics Letters* **2013,** 103, (9), 093108.
18. Gomes, L. C.; Carvalho, A. *Physical Review B* **2015,** 92, (8), 085406.
19. Steinmann, V.; Jaramillo, R.; Hartman, K.; Chakraborty, R.; Brandt, R. E.; Poindexter, J. R.; Lee, Y. S.; Sun, L.; Polizzotti, A.; Park, H. H.; Gordon, R. G.; Buonassisi, T. *Advanced Materials* **2014,** 26, (44), 7488-7492.
20. Zhao, L.-D.; Lo, S.-H.; Zhang, Y.; Sun, H.; Tan, G.; Uher, C.; Wolverton, C.; Dravid, V. P.; Kanatzidis, M. G. *Nature* **2014,** 508, (7496), 373-377.
21. Biacchi, A. J.; Vaughn, D. D.; Schaak, R. E. *Journal of the American Chemical Society* **2013,** 135, (31), 11634-11644.
22. Herron, S. M.; Tanskanen, J. T.; Roelofs, K. E.; Bent, S. F. *Chemistry of Materials* **2014,** 26, (24), 7106-7113.
23. Liu, X.; Li, Y.; Zhou, B.; Wang, X.; Cartwright, A. N.; Swihart, M. T. *Chemistry of Materials* **2014,** 26, (11), 3515-3521.

24. Burton, L. A.; Colombara, D.; Abellon, R. D.; Grozema, F. C.; Peter, L. M.; Savenije, T. J.; Dennler, G.; Walsh, A. *Chemistry of Materials* **2013,** 25, (24), 4908-4916.
25. Krasheninnikov, A. V.; Banhart, F. *Nature Materials* **2007,** 6, (10), 723-733.
26. Krasheninnikov, A. V.; Nordlund, K. *Journal of Applied Physics* **2010,** 107, (7), 071301.
27. Zhou, T.; Pang, W. K.; Zhang, C.; Yang, J.; Chen, Z.; Liu, H. K.; Guo, Z. *ACS Nano* **2014,** 8, (8), 8323-8333.
28. Kotakoski, J.; Jin, C. H.; Lehtinen, O.; Suenaga, K.; Krasheninnikov, A. V. *Physical Review B* **2010,** 82, (11), 113404.
29. Cretu, O.; Lin, Y.-C.; Suenaga, K. *Micron* **2015,** 72, 21-27.
30. Alem, N.; Erni, R.; Kisielowski, C.; Rossell, M. D.; Gannett, W.; Zettl, A. *Physical Review B* **2009,** 80, (15), 155425.
31. Björkman, T. *The Journal of Chemical Physics* **2014,** 141, (7), 074708.
32. Hamada, I. *Physical Review B* **2014,** 89, (12), 121103.
33. Sharma, R. C.; Chang, Y. A. *Bulletin of Alloy Phase Diagrams* 7, (3), 269-273.
34. Sharma, R. C.; Chang, Y. A. *Bulletin of Alloy Phase Diagrams* 7, (1), 68-72.
35. Jung, Y.; Shen, J.; Liu, Y.; Woods, J. M.; Sun, Y.; Cha, J. J. *Nano Letters* **2014,** 14, (12), 6842-6849.
36. Ghorbani-Asl, M.; Borini, S.; Kuc, A.; Heine, T. *Physical Review B* **2013,** 87, (23), 235434.
37. Jaramillo, T. F.; Jørgensen, K. P.; Bonde, J.; Nielsen, J. H.; Horch, S.; Chorkendorff, I. *Science* **2007,** 317, (5834), 100-102.
38. Li, Y.; Wang, H.; Xie, L.; Liang, Y.; Hong, G.; Dai, H. *Journal of the American Chemical Society* **2011,** 133, (19), 7296-7299.
39. Seo, J.-w.; Jang, J.-t.; Park, S.-w.; Kim, C.; Park, B.; Cheon, J. *Advanced Materials* **2008,** 20, (22), 4269-4273.
40. Kim, T.-J.; Kim, C.; Son, D.; Choi, M.; Park, B. *Journal of Power Sources* **2007,** 167, (2), 529-535.
41. Zhang, C.; Yin, H.; Han, M.; Dai, Z.; Pang, H.; Zheng, Y.; Lan, Y.-Q.; Bao, J.; Zhu, J. *ACS Nano* **2014,** 8, (4), 3761-3770.
42. Sharp, L.; Soltz, D.; Parkinson, B. A. *Crystal Growth & Design* **2006,** 6, 1523-1527.
43. Huang, Y.; Sutter, E.; Shi, N. N.; Zheng, J.; Yang, T.; Englund, D.; Gao, H.-J.; Sutter, P. *ACS Nano* **2015,** 9, (11), 10612-10620.
44. Kresse, G.; Hafner, J. *Physical Review B* **1993,** 47, (1), 558-561.
45. Kresse, G.; Furthmüller, J. *Computational Materials Science* **1996,** 6, (1), 15-50.
46. Perdew, J. P.; Zunger, A. *Physical Review B* **1981,** 23, (10), 5048-5079.
47. Perdew, J. P.; Burke, K.; Ernzerhof, M. *Physical Review Letters* **1996,** 77, (18), 3865-3868.
48. Grimme, S. *Journal of Computational Chemistry* **2006,** 27, (15), 1787-1799.

TOC Graphic